Constrained Visibility Guidance for 6-DOF Powered Descent Maneuvers with Terrain Scanning using Sequential Convex Programming

Samuel C. Buckner* and Behçet Açıkmeşe†
University of Washington, Seattle, WA 98195, USA

Joshua Shaffer‡
Astrobotic Technology, Pittsburgh, PA 15233, USA

John M. Carson III§, Breanna J. Johnson¶ and Ronald R. Sostaric‖
NASA Johnson Space Center, Houston, TX 77058, USA

Recent advances in perceptive sensors and computer vision have motivated new formulations for powered descent guidance, wherein a vehicle must perform a pinpoint landing on a celestial body while simultaneously conducting close-range scans of the landing environment to detect and avoid potentially-unsafe hazards. Furthermore, mission plans may necessitate exploration and scouting of the environment to determine candidate landing sites in real time. In this paper, a novel six degree-of-freedom (6-DOF) optimal control formulation is presented to model visibility-based constraints such that line-of-sight to a circular ground-based region of interest is guaranteed, up to a specified discrete temporal resolution, with an accommodating theory of constrained conic intersections introduced to support this approach. This formulation, termed Constrained Visibility Guidance (CVG), further leverages and extends theory in sequential convex programming and state-triggered constraints to enable mission-practical constraint specification and transformation of a highly-nonconvex problem into one that can be iteratively solved with modern second-order cone program solvers. Ultimately, CVG is shown to be highly performant in terms of solve time and convergence properties, even under complex and highly-constrained problem design. Numerical simulation results are presented to validate these claims.

I. Nomenclature

$\mathcal{I}$	Inertially-fixed frame of reference (inertial frame)
$\mathcal{B}$	Body-fixed frame of reference (body frame)
$\mathcal{F}$	Arbitrary frame of reference
$R_{\mathcal{F}_1 \to \mathcal{F}_2}$	Rotation matrix from frame $\mathcal{F}_1$ to frame $\mathcal{F}_2$
$\{e_x, e_y, e_z\}$	Standard basis, equivalent to $\{e_1, e_2, e_3\}$
SO(3)	Special orthogonal group in three-dimensional space
$[n]$	Shorthand notation, equivalent to $1, \ldots, n$
$\|\cdot\|$	Norm operation, assumed to be Euclidean (two) norm by default
3-DOF	Three degree-of-freedom point-mass dynamics (translation-only)
6-DOF	Six degree-of-freedom point-mass dynamics (translation and rotation)
CVG	Constrained Visibility Guidance
PDG	Powered Descent Guidance
SOC	Second-order cone

*NSF Fellow, William E. Boeing Dept. of Aeronautics & Astronautics, AIAA Student Member; sbuckne1@uw.edu.
†Professor, William E. Boeing Dept. of Aeronautics & Astronautics, AIAA Fellow; behcet@uw.edu.
‡GNC Engineer; joshua.shaffer@astrobotic.com.
§Technical Integration Manager – Precision Landing, NASA STMD, AIAA Associate Fellow; john.m.carson@nasa.gov.
¶Aerospace Engineer, Flight Mechanics and Trajectory Design Branch, AIAA Atmospheric Flight Mechanics Technical Committee Member; breanna.j.johnson@nasa.gov.
‖Aerospace Engineer, Flight Mechanics and Trajectory Design Branch, AIAA Senior Member; ronald.r.sostaric@nasa.gov.

II. Introduction

Substantial modern developments have been made to the field of powered descent guidance (PDG), which concerns the theoretical and algorithmic design of pinpoint landing strategies on celestial bodies under critical hardware-driven constraints. Recent contributions have focused on the adoption of numerical optimization and convexification to this problem through direct collocation approaches focused on a minimum-fuel optimality criterion. The first development under this class of techniques was coined "lossless convexification" [1–6], which provides continuous-time optimality guarantees for a special class of nonconvex constraints [2], including control magnitude lower bounds and thrust pointing constraints, such that the converged solution is *lossless* (meaning global optimality to the original nonconvex problem is obtained). This property enables adoption of algorithms embedding lossless convexification in real-time onboard rocketry operations [7, 8], evidenced by a successful sequence of flight tests onboard the Xombie vehicle as part of the G-FOLD program [9–11]. While more recent developments have been made to lossless convexification theory, including embedding of linear and quadratic state constraints [5, 6], semi-continuous inputs [12, 13] and annular input constraints [14], this research is still typically restricted to three degree-of-freedom (3-DOF) dynamics models strictly in terms of vehicle translational motion.

More recently, the theory of successive convexification [15, 16], classed underneath a family of algorithms known as Sequential Convex Programming (SCP) [17–19], has been introduced to the field of nonconvex optimal control and trajectory planning. These methods encapsulate a class of iterative convex-approximation-based techniques (typically using first-order linearization), which provide flexibility towards arbitrarily-complex constraint modeling at the expense of local optimality convergence and nontrivial hyperparameter tuning. Research conducted around these methods has enabled implementation of highly nonlinear six degree-of-freedom (6-DOF) dynamics for the PDG problem using standard quaternion [20–22] and dual quaternion [23] models, in addition to other formulations [24, 25]. The dual quaternion-based SCP approach, built on previous research [26–28], is additionally in contention as the core guidance algorithm for the NASA SPLICE program [29]. Other research has targeted general performance characterization and improvements of SCP in these problem contexts [30–32], as well as implementation with a first-order convex solver for faster real-time performance [33–35]. A substantial amount of literature also exists providing an introduction and canonicalization of both lossless and successive convexification/SCP in the optimal control context [36, 37].

The problem of *hazard-aware* powered descent guidance concerns an extension to the hallmark pinpoint landing problem where the vehicle must also maintain conditional sensor line-of-sight to the target landing site. This problem is motivated by the need for close-range terrain scanning using a perceptive sensor (e.g. camera or LiDAR) while descending to obtain information about possible hazards that were not known *a priori* (hence making the approach hazard-aware). Recent approaches include SCP-based methods which directly constrain the angle between the sensor boresight vector and landing site directional vector and condition the constraint on a state-based trigger set, such as a minimum and maximum range to the landing site (as in [23, 34]) – this class of constraints is typically referred to as State-Triggered Constraints (STCs). Notably, this formulation is restricted to guaranteeing visibility of a singular point located at the origin. In this paper, a new formulation, termed Constrained Visibility Guidance (CVG), is proposed which contains the following novel extensions to aforementioned literature:

1) A new CVG-specific constraint set is formulated which enables guaranteed sensor line-of-sight to an *entire* circular region of interest (rather than a single point) with arbitrary centroid location and radius. Furthermore, an approximation is introduced which enables extraction of a closed-form solution and facilitates generalization to guaranteed visibility of any set that can be reasonably approximated with a 2-norm ball. It is noted that this constraint type is also introduced in a 3-DOF lossless convexification format in [38], however with substantial restrictions on the feasible search space.
2) A new theory of constrained conic intersections is introduced which validates the closed-form solution of the 2-norm ball approximated CVG constraint set mentioned previously.
3) An integrated formulation of various state-of-the-art techniques in SCP modeling and optimal control is developed and catered to the mission-practical specification of terrain scanning events.
4) A methodology for initialization of SCP algorithms under this problem class is presented which facilitates conversion of any 3-DOF solution to a proximal 6-DOF solution.

The remainder of this paper is outlined as follows. Section III introduces the canonical continuous-time optimal control formulation. Section IV justifies the CVG line-of-sight constraint set through theoretical rigour. Section V leverages direct multiple-shooting discretization and sequential convex programming to convert the aforementioned formulation to a problem that is tractable in real-time with modern numerical solvers. Section VI presents simulation and analysis results on a candidate mission scenario for powered descent guidance with terrain scanning objectives. Finally, section VII concludes all discussion and presents next steps in regards to theoretical and practical considerations of CVG.

III. Problem Formulation

We begin by outlining the necessary construction for the 6-DOF constrained visibility guidance (CVG) problem. The formulation shares many resemblances to 6-DOF approaches found in the literature (particularly [21]), along with its own key distinctions in terms of dynamics and constraint modeling. We consider the following two reference frames for the remainder of the paper:

- $\mathcal{I}$: An inertially-fixed Up-East-North reference frame with the origin located at the landing site.
- $\mathcal{B}$: A body-fixed reference frame with $+x$ pointing in the direction of the thrust vector $T(t)$, $+y$ pointing out the side of the vehicle, and $+z$ completing the right-handed system.

We note that the definition for frame $\mathcal{B}$ implies that the vehicle engine is non-gimbaled; this assumption will be used throughout the remainder of the paper, however gimbaling constraint models can be applied without loss of generality. Additionally, the choice of $+y$ is arbitrary provided it is perpendicular to $+x$, since the vehicle can roll freely about $+x$.

A. Dynamics

The dynamics model follows a standard quaternion-based 6-DOF formulation for the powered descent guidance problem as in [21]. The vehicle state $x(t) \in \mathbb{R}^{n_x}$ consists of a vertical concatenation of vehicle mass $m(t) \in \mathbb{R}$, inertial position $r_{\mathcal{I}}(t) \in \mathbb{R}^3$, inertial velocity $v_{\mathcal{I}}(t) \in \mathbb{R}^3$, body-relative unit quaternion attitude $q_{\mathcal{I}\to\mathcal{B}}(t) \in \mathbb{R}^4$ and body-fixed angular velocity $\omega_{\mathcal{B}}(t) \in \mathbb{R}^3$, with $n_x = 14$. Furthermore, the vehicle control $u(t) \in \mathbb{R}^{n_u}$ consists of a vertical concatenation of body-fixed thrust $T_{\mathcal{B}}(t) \in \mathbb{R}^3$ (under a single-engine model) and body-fixed moment $M_{\mathcal{B}}(t) \in \mathbb{R}^3$ (applied through a reaction control system rather than through gimbaling), with $n_u = 6$. Time $t \in \mathbb{R}_+$ is bounded by $t_0 = 0$ and t_f, such that $t \in [0, t_f]$. The full system dynamics can be expressed as follows:

$$\textbf{Mass:} \qquad \dot{m}(t) = -\alpha \|T_{\mathcal{B}}(t)\|_2 \tag{1}$$

$$\textbf{Position:} \qquad \dot{r}_{\mathcal{I}}(t) = v_{\mathcal{I}}(t) \tag{2}$$

$$\textbf{Velocity:} \qquad \dot{v}_{\mathcal{I}}(t) = \frac{1}{m(t)} \mathcal{R}_{\mathcal{I}\to\mathcal{B}}^{\top}(t) T_{\mathcal{B}}(t) + g_{\mathcal{I}} \tag{3}$$

$$\textbf{Attitude:} \qquad \dot{q}_{\mathcal{I}\to\mathcal{B}}(t) = \frac{1}{2} \Omega\left(\omega_{\mathcal{B}}(t)\right) q_{\mathcal{I}\to\mathcal{B}}(t) \tag{4}$$

$$\textbf{Angular Velocity:} \qquad \dot{\omega}_{\mathcal{B}}(t) = J_{\mathcal{B}}^{-1}\left(M_{\mathcal{B}}(t) - [\omega_{\mathcal{B}}(t)\times] J_{\mathcal{B}} \omega_{\mathcal{B}}(t)\right) \tag{5}$$

Where $\alpha \in \mathbb{R}$ denotes the vehicle's engine proportionality constant in terms of vacuum-specific impulse $I_{\text{sp}} \in \mathbb{R}$ and Earth's standard gravity constant $g_0 \in \mathbb{R}$, $g_{\mathcal{I}} \in \mathbb{R}^3$ denotes the local gravitational acceleration expressed in the inertial frame, and $J_{\mathcal{B}} \in \mathbb{R}^{3\times 3}$ denotes the vehicle's moment of inertia matrix in the body frame. Additionally, the skew-symmetric matrix operations on an input vector $\xi \in \mathbb{R}^3$ are defined as follows:

$$[\xi\times] \triangleq \begin{bmatrix} 0 & -\xi_z & \xi_y \\ \xi_z & 0 & -\xi_x \\ -\xi_y & \xi_x & 0 \end{bmatrix} \qquad \Omega(\xi) \triangleq \begin{bmatrix} 0 & -\xi_x & -\xi_y & -\xi_z \\ \xi_x & 0 & \xi_z & -\xi_y \\ \xi_y & -\xi_z & 0 & \xi_x \\ \xi_z & \xi_y & -\xi_x & 0 \end{bmatrix}$$

Finally, an expression of the vehicle's attitude in terms of a direction cosine matrix, $\mathcal{R}_{\mathcal{I}\to\mathcal{B}}(t) \in \mathrm{SO}(3)$, is given by considering the following transformation from unit quaternion $q_{\mathcal{I}\to\mathcal{B}}(t) = [q_0, q_1, q_2, q_3]^{\top}$:

$$\mathcal{R}_{\mathcal{I}\to\mathcal{B}}(t) = \begin{bmatrix} 1-2(q_2^2+q_3^2) & 2(q_1q_2+q_0q_3) & 2(q_1q_3-q_0q_2) \\ 2(q_1q_2-q_0q_3) & 1-2(q_1^2+q_3^2) & 2(q_2q_3+q_0q_1) \\ 2(q_1q_3+q_0q_2) & 2(q_2q_3-q_0q_1) & 1-2(q_1^2+q_2^2) \end{bmatrix}$$

B. Continuous Time-Interval Dilation

The aforementioned dynamics are configured for a fixed-final-time problem with respect to the cumulative flight time t_f. In [21], the approach of time dilation was introduced to modify the dynamics and enable t_f to be expressed as a decision variable. In [34], time-*interval* dilation was introduced as an extension to this concept to enable the time at *all* discrete-time optimization knot points to be free variables. In this paper, we consider an alternate formulation of time-interval dilation, building off previous literature [39], that lends itself to a canonicalized continuous-time description.

We start by defining a continuous-time dynamics function mapping $f : (\mathbb{R} \times \mathbb{R}^{n_x} \times \mathbb{R}^{n_u}) \to \mathbb{R}^{n_x}$ such that $\dot{x}(t) \triangleq f(t, x(t), u(t))$. We will consider a normalized (dilated) time representation $\tau \in [0, 1]$, and consequently

define the wall-clock time t as a smooth monotonic mapping $t(\tau) : [0,1] \to [0,t_f]$. We can define the time derivative:

$$s(\tau) \triangleq \frac{dt(\tau)}{d\tau} > 0 \tag{6}$$

We will define (x,u) as the dilated state and control, and $(\tilde{x},\tilde{u})$ as their non-dilated counterparts. Using the chain rule, we can express our dynamics as follows:

$$\mathring{\tilde{x}}(t(\tau)) = \frac{d\tilde{x}(t(\tau))}{d\tau} = \frac{d\tilde{x}(t(\tau))}{dt(\tau)}\frac{dt(\tau)}{d\tau} = s(\tau)f(t(\tau),\tilde{x}(t(\tau)),\tilde{u}(t(\tau))) \tag{7}$$

Finally, we arrive at our dilated dynamics relationship defined by a function $g : (\mathbb{R}\times\mathbb{R}^{n_x}\times\mathbb{R}^{n_u}) \to \mathbb{R}^{n_x}$ such that:

$$\mathring{x}(\tau) = g(\tau, x(\tau), \nu(\tau)) \tag{8}$$

Where relationships are defined such that g evolves over τ, and the time dilation term $s(\tau)$ has been restructured into the control input by defining an augmented control ν (allowing this formulation to be amenable to canonical discretization techniques), such that we have:

$$x(\tau) = \tilde{x}(t(\tau)) \tag{9}$$
$$u(\tau) = \tilde{u}(t(\tau)) \tag{10}$$
$$\nu(\tau) = \begin{bmatrix} u(\tau) \\ s(\tau) \end{bmatrix} \tag{11}$$
$$g(\tau, x(\tau), \nu(\tau)) = s(\tau)f(t(\tau),\tilde{x}(t(\tau)),\tilde{u}(t(\tau))) \tag{12}$$

As a note, for any dilated time τ, there exists a mapping to time t defined as follows:

$$t(\tau) = \int_0^\tau s(\theta)\mathrm{d}\theta \tag{13}$$

C. Constrained Visibility Guidance (CVG) Constraints

We start by considering a body-fixed boresight vector $b_{\mathcal{B}} \in \mathbb{R}^3$ (with unit magnitude) associated with a vision-based sensor onboard the vehicle (such as the central pointing direction of a camera or LiDAR-based system), coupled with a field-of-view (FOV) half-angle $\beta \in \mathbb{R}$. The prototypical boresight pointing constraint seeks to align the vehicle's boresight vector towards the relative direction of a point $z \in \mathbb{R}^3$ (which may represent a landing site or some other point-of-interest) such that the angle between the boresight vector and relative direction $z - r(t)$ is less than β (moreover, such that the point z is in the field of view of the vehicle's vision sensor). This constraint can be formally constructed as a *biconic* constraint in $r_{\mathcal{I}}(t)$ and $b_{\mathcal{I}}(t)$ (that is, the constraint defines a convex cone in each variable if the other is held constant; in this case, a second-order cone, specifically). We will denote this constraint set by $\mathcal{F}(z)$:

$$\mathcal{F}(z) = \left\{ (r_{\mathcal{I}}(t), b_{\mathcal{I}}(t)) \mid \|z_{\mathcal{I}} - r_{\mathcal{I}}(t)\| \leq \frac{(z_{\mathcal{I}} - r_{\mathcal{I}}(t))^\top b_{\mathcal{I}}(t)}{\cos\beta} \right\} \tag{14}$$

Where $b_{\mathcal{I}}(t) = \mathcal{R}^\top_{\mathcal{I}\to\mathcal{B}}(t)b_{\mathcal{B}}$. If we instead choose to consider a *region* of interest $\mathcal{Z} \subseteq \mathbb{R}^3$, we can extend this definition as such:

$$\mathcal{F}(\mathcal{Z}) = \left\{ (r_{\mathcal{I}}(t), b_{\mathcal{I}}(t)) \mid \|\tilde{z}_{\mathcal{I}} - r_{\mathcal{I}}(t)\| \leq \frac{(\tilde{z}_{\mathcal{I}} - r_{\mathcal{I}}(t))^\top b_{\mathcal{I}}(t)}{\cos\beta},\ \forall \tilde{z} \in \mathcal{Z} \right\} \tag{15}$$
$$= \bigcap_{\tilde{z}\in\mathcal{Z}} \left\{ (r_{\mathcal{I}}(t), b_{\mathcal{I}}(t)) \mid \|\tilde{z}_{\mathcal{I}} - r_{\mathcal{I}}(t)\| \leq \frac{(\tilde{z}_{\mathcal{I}} - r_{\mathcal{I}}(t))^\top b_{\mathcal{I}}(t)}{\cos\beta} \right\} \tag{16}$$

For most forms of $\mathcal{Z}$, the above equation may not have a closed-form solution, and cannot otherwise be expressed as a tractable set of constraints in a numerical optimization problem if $\mathcal{Z}$ is uncountably-infinite. In the case of the powered descent guidance problem, we may seek to consider a circular region of interest on the ground, with radius ρ, constrained to the inertial x-y plane (under a flat-terrain model), denoted as the set $\mathcal{Z}_{\text{circ}} \subseteq \mathbb{R}^3$ with form:

$$\mathcal{Z}_{\text{circ}} \triangleq \{\tilde{z} \in \mathbb{R}^3 \mid \|H(z - \tilde{z})\| \leq \rho\}, \qquad H = \begin{bmatrix} 1 & 0 & 0 \\ 0 & 1 & 0 \end{bmatrix} \tag{17}$$

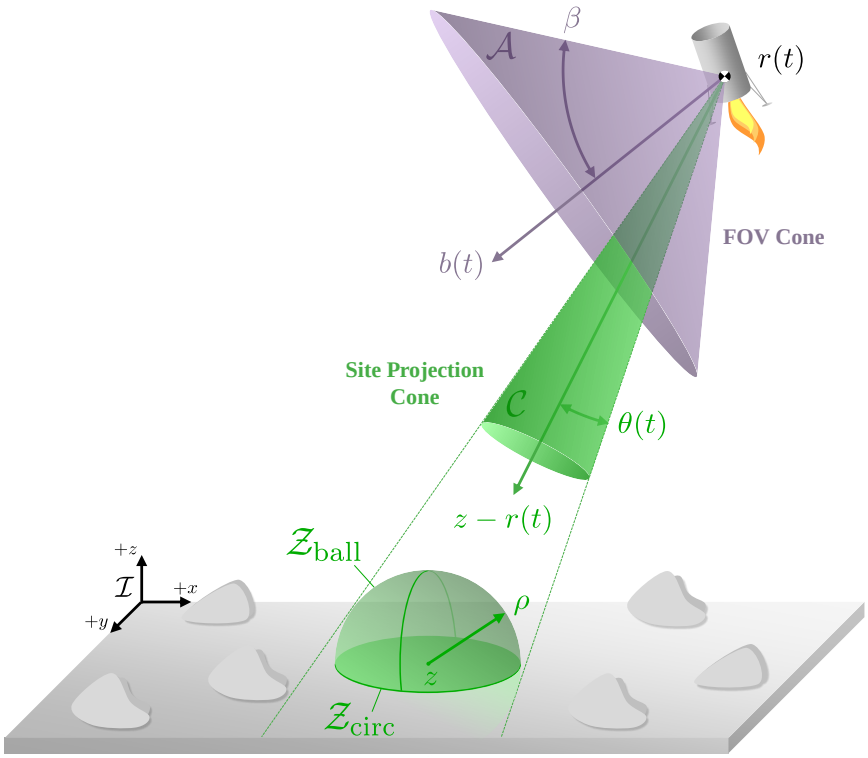

Fig. 1 An illustration of the problem geometry underlying the CVG-specific constraint definitions.

Where H denotes the projection matrix onto the terrain plane. The constraint set we ultimately wish to enforce is $\mathcal{F}(\mathcal{Z}_{\text{circ}})$, however this set does not lend itself to a convenient closed-form solution. An approximation can be formed, however, by instead considering the unit ball $\mathcal{Z}_{\text{ball}}$ which circumscribes $\mathcal{Z}_{\text{circ}}$:

$$\mathcal{Z}_{\text{ball}} \triangleq \{\tilde{z} \in \mathbb{R}^3 \mid \|z - \tilde{z}\| \leq \rho\} \tag{18}$$

This approximation will henceforth be termed the "ball approximation" on the landing site region $\mathcal{Z}_{\text{circ}}$. We note that the set $\mathcal{Z}_{\text{ball}}$ acts as a conservative overapproximation of the original set $\mathcal{Z}_{\text{circ}}$ (since $\mathcal{Z}_{\text{circ}} \subset \mathcal{Z}_{\text{ball}}$), and consequently introduces further restrictions on the feasible set from the definition of an intersection:

$$\mathcal{Z}_{\text{circ}} \subset \mathcal{Z}_{\text{ball}} \implies \mathcal{F}(\mathcal{Z}_{\text{circ}}) \supseteq \mathcal{F}(\mathcal{Z}_{\text{ball}})$$

Even after this approximation, the set $\mathcal{F}(\mathcal{Z}_{\text{ball}})$ remains difficult to be reduced to a tractable closed-form constraint set. We can instead re-imagine this problem by considering the rays which extend from some $r_{\mathcal{I}}(t)$ towards all points in $\mathcal{Z}_{\text{ball}}$, denoted as $\xi \in \mathbb{R}^3$. Geometrically, this set represents a second-order cone (SOC) pointing in the direction $z_{\mathcal{I}} - r_{\mathcal{I}}(t)$ with a half-angle $\theta(t)$ such that the cone has a cross-section at distance $\|z_{\mathcal{I}} - r_{\mathcal{I}}(t)\|$ corresponding to $\mathcal{Z}_{\text{ball}}$ (that is, this set defines the cone that *projects* to $\mathcal{Z}_{\text{ball}}$). This set, denoted $\mathcal{C}_{\text{cvg}}$, can be stated as:

$$\mathcal{C}_{\text{cvg}} = \left\{ (r_{\mathcal{I}}(t), \xi) \mid \|z_{\mathcal{I}} - r_{\mathcal{I}}(t)\| \|\xi\| \leq \frac{(z_{\mathcal{I}} - r_{\mathcal{I}}(t))^\top \xi}{\cos\theta(t)} \right\} \tag{19}$$

Where:

$$\theta(t) = \arctan\left(\frac{\rho}{\|z_{\mathcal{I}} - r_{\mathcal{I}}(t)\|}\right) \tag{20}$$

Where $\theta(t)$ can be derived from simple trigonometric relations. We can also consider the set defining the sensor FOV cone, which can be simply stated as the set $\mathcal{A}_{\text{cvg}}$:

$$\mathcal{A}_{\text{cvg}} = \left\{ (b_{\mathcal{I}}(t), \xi) \mid \|\xi\| \leq \frac{b_{\mathcal{I}}(t)^\top \xi}{\cos\beta} \right\} \tag{21}$$

A visualization of both sets $\mathcal{A} = \mathcal{A}_{\text{cvg}}$ and $\mathcal{C} = \mathcal{C}_{\text{cvg}}$ is provided in Fig. 1 for a fixed $r_{\mathcal{I}}(t)$ and $b_{\mathcal{I}}(t)$. The problem we would like to formally pose is to find all $r_{\mathcal{I}}(t), b_{\mathcal{I}}(t) \in \mathbb{R}^3$ such that $\mathcal{C}_{\text{cvg}} \subseteq \mathcal{A}_{\text{cvg}}$. Informally, this means that

the FOV cone $\mathcal{A}_{\text{cvg}}$ obtains full coverage of the approximate landing site region $\mathcal{Z}_{\text{ball}}$, since $\mathcal{C}_{\text{cvg}}$ projects to $\mathcal{Z}_{\text{ball}}$. This is equivalent to finding the set $\mathcal{B}_{\text{cvg}}$ in $(r_{\mathcal{I}}(t), b_{\mathcal{I}}(t))$ that satisfies the following relationship:

$$\bigcap_{\xi \in \mathcal{C}_{\text{cvg}}} \mathcal{A}_{\text{cvg}} = \mathcal{B}_{\text{cvg}} \tag{22}$$

It can be shown that the set $\mathcal{B}_{\text{cvg}}$ has the following form:

$$\mathcal{B}_{\text{cvg}} = \left\{ (r_{\mathcal{I}}(t), b_{\mathcal{I}}(t)) \mid \|z_{\mathcal{I}} - r_{\mathcal{I}}(t)\| \leq \frac{(z_{\mathcal{I}} - r_{\mathcal{I}}(t))^\top b_{\mathcal{I}}(t)}{\cos(\beta - \theta(t))} \right\} \tag{23}$$

Where a rigorous theoretical proof for this relationship can be found in the following section IV. We note that this constraint set is almost identical to the original pointing constraint to a single point (14), with the $\cos\beta$ term replaced by a $\cos(\beta - \theta(t))$ term (which provides direct quantification of the further reduction in feasible space to impose this constraint). Finally, this constraint set is only valid to impose if the vehicle's relative position is large enough to capture the entire region of interest within the sensor field-of-view (such that $\beta > \theta(t)$). Formally, this consideration can be imposed as an additional constraint:

$$\|z_{\mathcal{I}} - r_{\mathcal{I}}(t)\| > \frac{\rho}{\tan\beta} \tag{24}$$

Which can be approximated as:

$$\frac{\rho}{\tan\beta} - \|z_{\mathcal{I}} - r_{\mathcal{I}}(t)\| \leq \epsilon \tag{25}$$

Where $\epsilon \approx 1e-6$ to encode a tractable inequality constraint (since strict inequalities cannot be traditionally imposed in numerical solvers). We will additionally impose a restriction that $\beta < \pi/2$ which is generally reasonable for practical purposes.

D. Other State and Control Constraints

The remainder of constraints considered in this specific problem definition are reasonably standard for powered descent guidance applications, and can be considered independent of the CVG constraint set introduced above. In terms of state constraints, we first consider bounds on velocity terms. Moreover, translational velocity, $v_{\mathcal{I}}(t)$, and angular velocity, $\omega_{\mathcal{I}}(t)$, are upper bounded by terms $v_{\max}$ and $\omega_{\max}$, respectively, as follows:

$$\|v_{\mathcal{I}}(t)\| \leq v_{\max} \tag{26}$$
$$\|\omega_{\mathcal{I}}(t)\| \leq \omega_{\max} \tag{27}$$

Additionally, a minimum altitude constraint is specified to ensure the vehicle does not fly below the terrain (alternatively, a glide-slope constraint, as used in [4], could also be considered):

$$e_z^\top r_{\mathcal{I}}(t) \geq 0 \tag{28}$$

In terms of control constraints, we consider upper bounds on both thrust, $T_{\mathcal{B}}(t)$, and torque, $M_{\mathcal{B}}(t)$, with respect to quantities $T_{\max}$ and $M_{\max}$, respectively, as follows:

$$\|T_{\mathcal{B}}(t)\| \leq T_{\max} \tag{29}$$
$$\|M_{\mathcal{B}}(t)\| \leq M_{\max} \tag{30}$$

We additionally consider a lower bound on thrust to account for standard engine minimum throttling limitations with quantity $T_{\min}$ as follows:

$$T_{\min} \leq \|T_{\mathcal{B}}(t)\| \tag{31}$$

Finally, to ensure the vehicle's thrust is constrained to the body frame $+x$ axis (given that it is non-gimbaled), we further constrain the thrust as follows:

$$e_x^\top T_{\mathcal{B}}(t) \geq 0 \tag{32}$$
$$e_y^\top T_{\mathcal{B}}(t) = 0 \tag{33}$$
$$e_z^\top T_{\mathcal{B}}(t) = 0 \tag{34}$$

E. Boundary Conditions

In terms of boundary conditions, each state term must be handled separately. The initial mass of the vehicle is set to be the mass at the beginning of the maneuver, $m_0 \in \mathbb{R}$, whereas the terminal mass is left as a free variable, lower-bounded by the minimum allowable remaining mass at the end of the maneuver, m_{min}:

$$m(0) = m_0 \tag{35}$$
$$m(t_f) \geq m_{\text{min}} \tag{36}$$

Position, velocity and angular velocity are equality-constrained at both initial and terminal times as follows:

$$r(0) = r_0, \qquad r(t_f) = r_f \tag{37}$$
$$v(0) = v_0, \qquad v(t_f) = v_f \tag{38}$$
$$\omega(0) = \omega_0, \qquad \omega(t_f) = \omega_f \tag{39}$$

The main distiction, with respect to previous literature, is in the specification of attitude boundary conditions. Due to the inclusion of the CVG constraints, we opted to leave attitude free both at initial and terminal times. However, while quaternion dynamics (given by equation (4)) are *norm-preserving*, they require restriction of quaternion magnitude to unity at *at least one* point in time. Thus, the following constraint must also be applied ($t = 0$ is chosen here):

$$\|q_{\mathcal{I}\to\mathcal{B}}(0)\| = 1 \tag{40}$$

F. State-Triggered Constraints

The CVG constraint set highlighted in equations (23) and (25) enables guaranteed terrain scanning of a region of interest $\mathcal{Z}_{\text{ball}}$, however in traditional mission operations, these visibility constraints do not need to be applied at all times $t \in [0, t_f]$. Moreover, attempting to do so may lead to infeasible problems, leading to the importance of state-triggered constraints (STCs), which are constraints triggered conditionally based off an evaluated criterion as a function of state $x(t)$. We consider the compound STC formulation introduced in [22], wherein $g(\cdot)$ is a trigger function and $c^j(\cdot), j \in [n_c]$ are a series of constraint functions (with n_c being the number of constraints to conditionally apply), with the following condition to be enforced:

$$g(x(t)) \leq 0 \implies \bigwedge_{j=1}^{n_c} c^j(x(t)) \leq 0 \tag{41}$$

In this paper, we propose an extension to the single-crossing trigger constraint set formulated in [34]. We consider a number of events n_{event} where, for each event $j \in [n_{\text{event}}]$, we have an event activation trigger g_j^+ and deactivation trigger g_j^-, with associated trigger times t_j^+ and t_j^-. We further require that these trigger conditions be strictly monotonic* and feasible:

$$0 \leq t_j^+ < t_j^- \leq t_f \tag{42}$$
$$g_j^- < g_j^+ \leq 0 \tag{43}$$

Then, we can impose the following constraint set $\forall j \in [n_{\text{event}}]$:

$$g_j^+(x(t)) \geq 0, \qquad \forall t \in [0, t_j^+] \tag{44}$$
$$g_j^+(x(t)) = 0, \qquad t = t_j^+ \tag{45}$$
$$g_j^+(x(t)) \leq 0, \qquad \forall t \in [t_j^+, t_j^-] \tag{46}$$
$$c^1(x(t)) \leq 0, \qquad \forall t \in [t_j^+, t_j^-] \tag{47}$$
$$\vdots$$
$$c^{n_c}(x(t)) \leq 0, \qquad \forall t \in [t_j^+, t_j^-] \tag{48}$$
$$g_j^-(x(t)) \geq 0, \qquad \forall t \in [t_j^+, t_j^-] \tag{49}$$
$$g_j^-(x(t)) = 0, \qquad t = t_j^- \tag{50}$$
$$g_j^-(x(t)) \leq 0, \qquad \forall t \in [t_j^-, t_f] \tag{51}$$

*We note that this condition is typically acceptable in the powered descent context when considering a trigger function such as altitude, which is typically expected to be monotonically decreasing with time. This approach is also exact in time, removing intersample constraint violations seen with previous methods. See [34] for a more in-depth explanation.

For our problem, we will consider n_{scan} separate terrain scanning events, with the two CVG constraints enforced for each event corresponding to a region of interest with centroid and radius $(z_{\mathcal{I}}^j, \rho^j)$, denoted as:

$$c^1(x(t)) = \|z_{\mathcal{I}}^j - r_{\mathcal{I}}(t)\| - \frac{(z_{\mathcal{I}}^j - r_{\mathcal{I}}(t))^\top \mathcal{R}_{\mathcal{I}\to\mathcal{B}}^\top(t) b_{\mathcal{B}}}{\cos(\beta - \theta^j(t))} \tag{52}$$

$$c^2(x(t)) = \frac{\rho^j}{\tan\beta} - \|z_{\mathcal{I}}^j - r_{\mathcal{I}}(t)\| - \epsilon \tag{53}$$

With:

$$\theta^j(t) = \arctan\left(\frac{\rho^j}{\|z_{\mathcal{I}}^j - r_{\mathcal{I}}(t)\|}\right) \tag{54}$$

As a shorthand, we will denote the application of triggers in equations (44)-(46) and (49)-(51) with the compound constraint $\mathcal{T}(g_j^+, g_j^-, t_j^+, t_j^-) \leq 0$.

G. Problem Statement

The resulting formulation using constraints garnered in sections III.A-III.F is presented in problem 55. This problem, as it stands, is a non-convex continuous-time problem; section V will present methods for convexification and discretization towards a tractable formulation for real-time numerical optimization. We also consider a generic objective function format with running cost Γ and terminal cost ϕ.

Non-Convex Continuous-Time Problem (55)

Objective:

$$\underset{x(\cdot),\nu(\cdot)}{\text{minimize}} \quad \phi(x(1)) + \int_0^1 \Gamma(x(\tau),\nu(\tau))\mathrm{d}t \tag{55a}$$

subject to: (55b)

Dynamics:

$$\mathring{x}(\tau) = g(x(\tau),\nu(\tau)) \qquad \forall \tau \in [0,1] \tag{55c}$$

State Constraints:

$$\|v_{\mathcal{I}}(\tau)\| \leq v_{\max} \qquad \forall \tau \in [0,1] \tag{55d}$$
$$\|\omega_{\mathcal{I}}(\tau)\| \leq \omega_{\max} \qquad \forall \tau \in [0,1] \tag{55e}$$
$$e_z^\top r_{\mathcal{I}}(\tau) \geq 0 \qquad \forall \tau \in [0,1] \tag{55f}$$

Control Constraints:

$$T_{\min} \leq \|T_{\mathcal{B}}(\tau)\| \leq T_{\max} \qquad \forall \tau \in [0,1] \tag{55g}$$
$$\|M_{\mathcal{B}}(\tau)\| \leq M_{\max} \qquad \forall \tau \in [0,1] \tag{55h}$$
$$e_x^\top T_{\mathcal{B}}(\tau) \geq 0 \qquad \forall \tau \in [0,1] \tag{55i}$$
$$e_y^\top T_{\mathcal{B}}(\tau) = e_z^\top T_{\mathcal{B}}(\tau) = 0 \qquad \forall \tau \in [0,1] \tag{55j}$$

Scanning STCs:

for $j \in [n_{\text{scan}}]$ (55k)

$$\|z_{\mathcal{I}}^j - r_{\mathcal{I}}(\tau)\| \leq \frac{(z_{\mathcal{I}}^j - r_{\mathcal{I}}(\tau))^\top \mathcal{R}_{\mathcal{I}\to\mathcal{B}}^\top(\tau) b_{\mathcal{B}}}{\cos(\beta - \theta(\tau))} \qquad \forall \tau \in [\tau_j^+, \tau_j^-] \tag{55l}$$

$$\frac{\rho^j}{\tan\beta} - \|z_{\mathcal{I}}^j - r_{\mathcal{I}}(\tau)\| \leq \epsilon \qquad \forall \tau \in [\tau_j^+, \tau_j^-] \tag{55m}$$

$$\mathcal{T}(g_j^+, g_j^-, \tau_j^+, \tau_j^-) \leq 0 \tag{55n}$$

end (55o)

Boundary Conditions:

$$m(0) = m_0, \quad m(1) \geq m_{\min} \tag{55p}$$
$$r_{\mathcal{I}}(0) = r_0, \quad r_{\mathcal{I}}(1) = r_f \tag{55q}$$
$$v_{\mathcal{I}}(0) = v_0, \quad v_{\mathcal{I}}(1) = v_f \tag{55r}$$
$$\omega_{\mathcal{B}}(0) = \omega_0, \quad \omega_{\mathcal{B}}(1) = \omega_f \tag{55s}$$
$$\|q_{\mathcal{I}\to\mathcal{B}}(0)\| = 1 \tag{55t}$$

IV. Theory of Constrained Conic Intersections

In this section, we consider the theory necessary to show the relationship established in (22). Moreover, we concern ourselves with determining the equivalence of two closed-form sets, wherein one set represents the infinite intersection of second-order cones. In theory, even the intersection of two second-order cones may not have an analytical closed-form solution under non-trivial conditions, however, it can be shown that this set equivalence can be made if the conic pointing vector of the intersected second-order cones is chosen as the varied parameter for the intersection operation, and this vector itself belongs to another second-order cone. For purely implementation purposes, this section can be ignored, however it provides the theoretical basis for this paper and could potentially lead to further theorems for more complicated sets in future research. This theorem is also used to support theoretical insights behind the control-robust envelope formulation in [38]. A visual interpretation of Theorem 1 is also provided in Fig. 2.

Theorem 1 (Intersection of Conics Constrained to a Conic)**.** *We seek to show that the following set equivalence for embedded intersection of second-order cones (SOCs) holds:*

$$\bigcap_{c\in\mathcal{C}} \left\{ x \in \mathbb{R}^3 \mid \|c\|\|x\| \leq \frac{c^\top x}{\cos\beta} \right\} = \left\{ x \in \mathbb{R}^3 \mid \|r\|\|x\| \leq \frac{r^\top x}{\cos(\beta-\theta)} \right\} \tag{56}$$

Where the set $\mathcal{C} \subseteq \mathbb{R}^3$ is defined as another SOC:

$$\mathcal{C} \triangleq \left\{ c \in \mathbb{R}^3 \mid \|r\| \|c\| \leq \frac{r^\top c}{\cos\theta} \right\} \tag{57}$$

And such that $r \in \mathbb{R}^3$ and $\theta, \beta \in \mathbb{R}$ are constant, where we can additionally impose the following angular constraints:

$$0 \leq \theta < \beta < \frac{\pi}{2}$$

Proof of Theorem 1. We can apply the shorthand set notation to the problem defined in equation (56):

$$\bigcap_{c \in \mathcal{C}} \mathcal{A}_c = \mathcal{B}$$

Where:

$$\mathcal{A}_c \triangleq \left\{ x \in \mathbb{R}^3 \mid \|c\| \|x\| \leq \frac{c^\top x}{\cos\beta} \right\}$$
$$\mathcal{B} \triangleq \left\{ x \in \mathbb{R}^3 \mid \|r\| \|x\| \leq \frac{r^\top x}{\cos(\beta - \theta)} \right\}$$

To show set equivalence, we must show the following two properties hold:

- **Set inclusivity condition ($\cap \mathcal{A}_c \supseteq \mathcal{B}$):** show that if $x \in \mathcal{B}$, then $x \in \mathcal{A}_c$ for every $c \in \mathcal{C}$.
- **Set exclusivity condition ($\cap \mathcal{A}_c \subseteq \mathcal{B}$):** show that if $x \notin \mathcal{B}$, then there exists some $c \in \mathcal{C}$ such that $x \notin \mathcal{A}_c$.

Part 1: set inclusivity condition. Consider the following linear decomposition of vector c to a basis $\{r, v, w\}$:

$$c = \alpha_r r + \alpha_v v + \alpha_w w \tag{58}$$

With $r \perp v$, $r \perp w$ and $v \perp w$. For some vector $c \in \mathcal{C}$, we can choose a proper $v \in \mathbb{R}^3$ such that $\alpha_w = 0$ and $\alpha_v \geq 0$ (polar coordinate representation), reducing the linear decomposition to:

$$c = \alpha_r r + \alpha_v v \tag{59}$$

For $c \in \mathcal{C}$, we have the following inequality relationship:

$$\cos\theta \leq \frac{r^\top c}{\|r\| \|c\|} \leq 1 \tag{60}$$

Under this relationship, we seek to show that the following property holds:

$$\frac{r^\top c}{\|r\| \|c\|} \geq \cos\theta \implies \left| \frac{v^\top c}{\|v\| \|c\|} \right| \leq \sin\theta \tag{61}$$

To do this, consider the right triangle formed by $\alpha_r r$, $\alpha_v v$ and c. We can define the angle between r and c as ϕ, and the angle between v and c as ψ, noting that under the right triangle, $\phi + \psi = \pi/2$. By definition, we also know that $\phi \leq \theta \implies \cos\phi \geq \cos\theta$, which forms the relationship:

$$\frac{r^\top c}{\|r\| \|c\|} = \cos\phi \geq \cos\theta \tag{62}$$

This consequently implies that $\psi \geq \pi/2 - \theta \implies \cos\psi \leq \cos(\pi/2 - \theta) = \sin\theta$. We also note that the angle ψ remains the same regardless of the signage of v. Thus we have the following relationships:

$$\frac{v^\top c}{\|v\| \|c\|} = \cos\psi \leq \sin\theta \tag{63}$$
$$-\frac{v^\top c}{\|v\| \|c\|} = \cos\psi \leq \sin\theta \tag{64}$$

Which, when combined, allow us to obtain the relationship described in (61). Then, we arrive at the following bounds:

$$-\sin\theta \leq \frac{v^\top c}{\|v\|\,\|c\|} \leq \sin\theta \tag{65}$$

By plugging in the decomposition of c from equation (59) into equations (60) and (65), we arrive at the following set of relationships in terms of the basis weights:

$$\frac{\|c\|}{\|r\|}\cos\theta \leq \alpha_r \leq \frac{\|c\|}{\|r\|} \tag{66}$$

$$0 \leq \alpha_v \leq \frac{\|c\|}{\|v\|}\sin\theta \tag{67}$$

Where we note that equation (66) implies $\alpha_r \geq 0$ (since $\cos\theta > 0$ when $\theta < \pi/2$), and that α_v is lower-bounded to zero due to the aforementioned domain restriction. We can then apply a similar linear decomposition of vector x with the same basis $\{r, v, w\}$:

$$x = \gamma_r r + \gamma_v v + \gamma_w w \tag{68}$$

(a) We start by constructing the second-order cone that defines the intersection operation, $\mathcal{C}$. This cone contains any $c \in \mathcal{C}$ that can be used to construct $\mathcal{A}_c$.

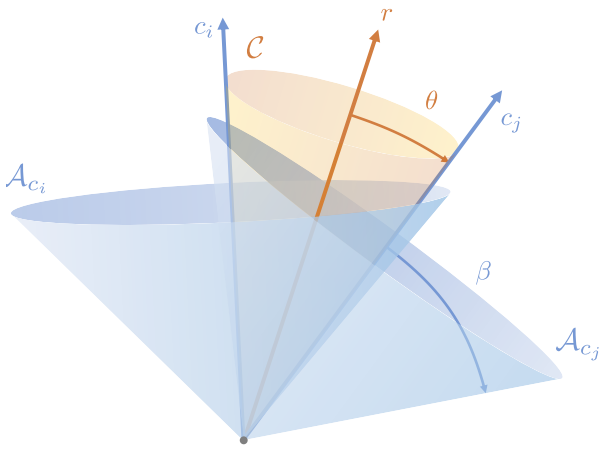

(b) We can then select two elements $c_i, c_j \in \mathcal{C}$ that are coplanar to r on the boundary of $\mathcal{C}$, and visualize their corresponding second-order cones $\mathcal{A}_{c_i}, \mathcal{A}_{c_j}$.

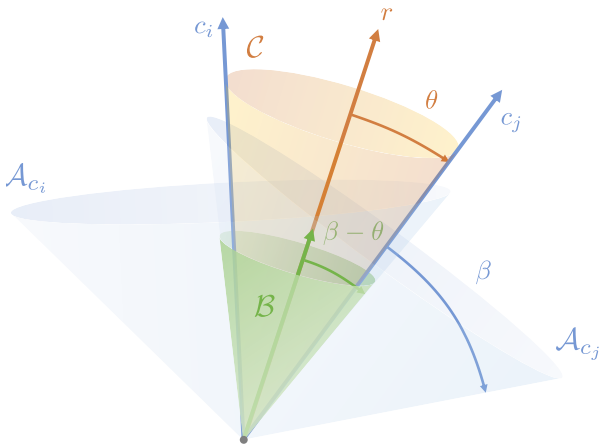

(c) The intersecting second-order cone, denoted as $\mathcal{B}$, is geometrically shown to have a half-angle of $\beta - \theta$ as stated by equation (56). We note that to truly visualize the intersecting set, we would need to consider all c_j in the boundary of $\mathcal{C}$ ($\text{int}(\mathcal{C})$ is not activated).

Fig. 2 A visual alternative to the proof provided in Theorem 1.

Then, we can use the definition of a vector $x \in \mathcal{B}$ to apply (56):

$$\cos(\beta - \theta) \leq \frac{r^\top x}{\|r\| \|x\|} \leq 1 \tag{69}$$

And apply the same argument used for (65) to arrive at the following relationships:

$$-\sin(\beta - \theta) \leq \frac{v^\top x}{\|v\| \|x\|} \leq \sin(\beta - \theta) \tag{70}$$

$$-\sin(\beta - \theta) \leq \frac{w^\top x}{\|w\| \|x\|} \leq \sin(\beta - \theta) \tag{71}$$

Consequently, we can plug in the decomposition of x from equation (68) into equations (69)-(71) to arrive at the following set of relationships in terms of basis weights:

$$\frac{\|x\|}{\|r\|} \cos(\beta - \theta) \leq \gamma_r \leq \frac{\|x\|}{\|r\|} \tag{72}$$

$$-\frac{\|x\|}{\|v\|} \sin(\beta - \theta) \leq \gamma_v \leq \frac{\|x\|}{\|v\|} \sin(\beta - \theta) \tag{73}$$

$$-\frac{\|x\|}{\|w\|} \sin(\beta - \theta) \leq \gamma_w \leq \frac{\|x\|}{\|w\|} \sin(\beta - \theta) \tag{74}$$

Where we note, once again, that equation (72) implies $\gamma_r \geq 0$ (since $\cos(\beta - \theta) > 0$ when $\beta - \theta < \pi/2$). Ultimately, we need to show that for any $c \in \mathcal{C}$ and $x \in \mathcal{B}$, that $x \in \mathcal{A}_c$, such that the following relationship is satisfied:

$$\cos\beta \leq \frac{c^\top x}{\|c\| \|x\|} \tag{75}$$

We can plug in the decompositions of c and x to arrive at the following relationship:

$$\frac{c^\top x}{\|c\| \|x\|} = \frac{\alpha_r \gamma_r \|r\|^2 + \alpha_v \gamma_v \|v\|^2}{\|c\| \|x\|} \tag{76}$$

Then, we can minimize the following relationship to obtain an inequality:

$$\min\left\{ \frac{\alpha_r \gamma_r \|r\|^2 + \alpha_v \gamma_v \|v\|^2}{\|c\| \|x\|} \right\} \leq \frac{c^\top x}{\|c\| \|x\|} \tag{77}$$

We have, by definition, that $\alpha_r, \alpha_v, \gamma_r \geq 0$ and $\gamma_v \in \mathbb{R},$. Then, to perform the minimization in equation (77), we need to minimize $\alpha_r, \gamma_r, \gamma_v$ and maximize α_v. We can use the previously-defined bounds on each term to do this; plugging in yields the following relationship:

$$\min\left\{ \frac{\alpha_r \gamma_r \|r\|^2 + \alpha_v \gamma_v \|v\|^2}{\|c\| \|x\|} \right\} \tag{78}$$

$$= \cos\theta \cos(\beta - \theta) - \sin\theta \sin(\beta - \theta) \tag{79}$$

$$= \cos\beta \tag{80}$$

Where the last relationship can be shown through trigonometric expansion. Therefore, we have that equation (75) is satisfied, and so the set inclusivity condition is shown.

Part 2: set exclusivity condition. We now wish to look at the case in which $x \notin \mathcal{B}$ such that:

$$\frac{r^\top x}{\|r\| \|x\|} < \cos(\beta - \theta) \tag{81}$$

We wish to find some $c \in \mathcal{C}$ such that $x \notin \mathcal{A}_c$, which means:

$$\frac{c^\top x}{\|c\| \|x\|} < \cos\theta \tag{82}$$

We can start by using the definition of the projection x onto r:

$$\text{proj}_r x = \frac{r^\top x}{r^\top r} r \tag{83}$$

We would like to consider the vector $c \in \mathcal{C}$ that is as "far away" from the vector x (in terms of angular displacement) as possible. In geometric consideration of this, we construct c on the boundary of $\mathcal{C}$ with a component perpendicular to r pointing in the direction of $- \perp \text{proj}_r x$ (defined under $\text{proj}_r x + \perp \text{proj}_r x = x$). We can once again consider a decomposition of c:

$$c = \alpha r - \perp \text{proj}_r x \tag{84}$$

$$= \alpha r + \frac{r^\top x}{r^\top r} r - x \tag{85}$$

Where α can be found using the following relationship:

$$\frac{r^\top c}{\|r\| \|c\|} = \cos\theta \tag{86}$$

$$\implies \frac{\|r\|}{\|c\|}\alpha + \frac{r^\top x}{\|r\| \|c\|} - \frac{r^\top x}{\|r\| \|c\|} = \cos\theta \tag{87}$$

$$\implies \alpha = \frac{\|c\|}{\|r\|} \cos\theta \tag{88}$$

We can then plug this into equation (82):

$$\frac{c^\top x}{\|c\| \|x\|} = \alpha \frac{r^\top x}{\|c\| \|x\|} + \frac{(r^\top x)^2}{\|c\| \|x\| \|r\|^2} - \frac{\|x\|}{\|c\|} \tag{89}$$

$$= \frac{r^\top x}{\|r\| \|x\|} \cos\theta + \frac{\|x\|}{\|c\|} \left(\frac{r^\top x}{\|r\| \|x\|} \right)^2 - \frac{\|x\|}{\|c\|} \tag{90}$$

$$< \cos\theta \cos(\beta - \theta) + \frac{\|x\|}{\|c\|} \cos^2(\beta - \theta) - \frac{\|x\|}{\|c\|} \tag{91}$$

$$= \cos\theta \cos(\beta - \theta) - \frac{\|x\|}{\|c\|} \sin^2(\beta - \theta) \tag{92}$$

$$\leq \cos\theta \tag{93}$$

Where the last relationship comes from the fact that $\cos(\beta - \theta) \leq 1$ and the subtracted term is strictly non-negative (since $\sin(\beta - \theta) > 0$). Thus, with the relationship posed by equation (82) satisfied, the set exclusivity condition is also shown.

□

A. Connection to the CVG Constraint Set

We can revisit the relationship in equation (22), which is stated in expanded form as follows:

$$\bigcap_{(r_\mathcal{I}(t), \xi) \in \mathcal{C}_{\text{cvg}}} \left\{ (b_\mathcal{I}(t), \xi) \mid \|\xi\| \leq \frac{\xi^\top b_\mathcal{I}(t)}{\cos\beta} \right\} = \left\{ (r_\mathcal{I}(t), b_\mathcal{I}(t)) \mid \|z_\mathcal{I} - r_\mathcal{I}(t)\| \leq \frac{(z_\mathcal{I} - r_\mathcal{I}(t))^\top b_\mathcal{I}(t)}{\cos(\beta - \theta(t))} \right\} \tag{94}$$

$$\mathcal{C}_{\text{cvg}} = \left\{ (r_\mathcal{I}(t), \xi) \mid \|z_\mathcal{I} - r_\mathcal{I}(t)\| \|\xi\| \leq \frac{(z_\mathcal{I} - r_\mathcal{I}(t))^\top \xi}{\cos\theta(t)} \right\} \tag{95}$$

Using Theorem 1, we can see that the above equivalence holds for *any* $r_\mathcal{I}(t) \in \mathbb{R}^n$ such that $\theta(t) < \beta$, which we explicitly constrained by imposing equation (25). Then, it follows that we can impose the right-hand side of the equivalence as an additional constraint even when $r_\mathcal{I}(t)$ is a decision variable, provided $r_\mathcal{I}(t)$ belongs to a valid domain enforced by equation (25).

V. Convexification and Transcription

In this section, we discuss a top-down reformulation of problem 55 such that it can be solved reliably and quickly using modern second-order cone program (SOCP) numerical optimization solvers. Moreover, we make use of the following two-step process commonly used in other literature [21, 36]:

1) **Convexification** through the use of sequential convex programming (SCP) techniques (specifically, a penalized trust region (PTR) method with *linearization* applied to nonconvex constraints).
2) **Transcription** using direct multiple shooting *discretization* with a first-order hold on the control input.

A. Linearization

For the remainder of the section, we will use $\hat{\square}$ to denote a reference quantity used in linearization, with the signal $(\hat{x}(\tau), \hat{u}(\tau))$ denoting the reference trajectory.

1. Dynamics

We can consider the time-interval-dilated dynamics relationship derived in equation (8) and obtain the following first-order Taylor series linearized variant evaluated at a time $\tau \in [0, 1]$:

$$\mathring{x}(\tau) = A(\tau)x(\tau) + B(\tau)\nu(\tau) + z(\tau) \tag{96}$$

Where each linearization matrix has the following form:

$$A(\tau) \triangleq \frac{\partial}{\partial x(\tau)} g(\tau, x(\tau), \nu(\tau))\bigg|_{(\hat{x}(\tau), \hat{\nu}(\tau))} \tag{97}$$

$$B(\tau) \triangleq \frac{\partial}{\partial \nu(\tau)} g(\tau, x(\tau), \nu(\tau))\bigg|_{(\hat{x}(\tau), \hat{\nu}(\tau))} \tag{98}$$

$$z(\tau) \triangleq -A(\tau)\hat{x}(\tau) - B(\tau)\hat{\nu}(\tau) \tag{99}$$

2. Other Constraints

In terms of nonconvex state constraints, we first consider the CVG constraint set. These constraints were earlier denoted in equations (52)-(53) with the functions $c^1(x(t))$ and $c^2(x(t))$. We can simply express the first-order Taylor series linearized constraints using an implicit representation (which can be resolved, in practice, using symbolic partial differentation algorithms):

$$C^1(\tau)\,(x(\tau) - \hat{x}(\tau)) + c^1(\hat{x}(\tau)) \leq 0 \tag{100}$$

$$C^2(\tau)\,(x(\tau) - \hat{x}(\tau)) + c^2(\hat{x}(\tau)) \leq 0 \tag{101}$$

Where, for $j = 1, 2$, we have that:

$$C^j(\tau) \triangleq \frac{\partial}{\partial x(\tau)} c^j(x(\tau))\bigg|_{\hat{x}(\tau)} \tag{102}$$

In regards to the quaternion norm boundary condition constraint expressed in equation (40), the linearization can be conveniently expressed by defining a norm derivative function $\Xi(\zeta) \triangleq \zeta/\|\zeta\|$, such that we have:

$$\Xi(\hat{q}_{\mathcal{I}\to\mathcal{B}}(0))^\top q_{\mathcal{I}\to\mathcal{B}}(0) = 1 \tag{103}$$

Similarly, for the one nonconvex control constraint – the thrust lower bound expressed in equation (31) – we can apply a similar linearization:

$$T_{\min} \leq \Xi(\hat{T}_{\mathcal{B}}(\tau))^\top T_{\mathcal{B}}(\tau) \tag{104}$$

B. Discretization

The first step in temporal discretization is to resolve the continuous dilated time domain $\tau \in [0, 1]$ into $N - 1$ partitions, such that we have a finite set of temporal points τ_k with $k = 1, \ldots, N$. While τ_k must be specified a-priori (typically with a uniform interpolation between $\{0, 1\}$), we note that due to the structure of time-interval dilation, all associated times t_k mapped by equation (13) are still free in terms of decision variables $\{s_k\}_{k=1}^N$.

Using the approach for first-order hold (FOH) dynamics discretization outlined in [31] – applied to our linearized time-interval-dilated dynamics expression in equation (96) – we can arrive at the following discretized variant (where $\xi_k \triangleq \xi(\tau_k)$ for notational convenience):

$$x_{k+1} = A_k x_k + B_k^- \nu_k + B_k^+ \nu_{k+1} + z_k \tag{105}$$

With the matrix terms defined as following (noting that $\Phi : (\mathbb{R} \times \mathbb{R}) \to \mathbb{R}^{n_x \times n_x}$ defines the *state transition matrix*):

$$A_k \triangleq \Phi(\tau_{k+1}, \tau_k), \tag{106}$$

$$B_k^- \triangleq A_k \int_{\tau_k}^{\tau_{k+1}} \Phi(\xi, \tau_k)^{-1} \lambda_k^-(\xi) B(\xi) \mathrm{d}\xi, \qquad \lambda_k^-(\tau) \triangleq \frac{\tau_{k+1} - \tau}{\tau_{k+1} - \tau_k} \tag{107}$$

$$B_k^+ \triangleq A_k \int_{\tau_k}^{\tau_{k+1}} \Phi(\xi, \tau_k)^{-1} \lambda_k^+(\xi) B(\xi) \mathrm{d}\xi, \qquad \lambda_k^+(\tau) \triangleq \frac{\tau - \tau_k}{\tau_{k+1} - \tau_k} \tag{108}$$

$$z_k \triangleq A_k \int_{\tau_k}^{\tau_{k+1}} \Phi(\xi, \tau_k)^{-1} z(\xi) \mathrm{d}\xi \tag{109}$$

C. Penalized Trust Region (PTR) Formulation

In regards to the use of the penalized trust region (PTR) algorithm, we consider the same formulation procedure presented in [21] (notably, we are omitting the "i" iterate notation for simplicity, and presenting an alternative formalization). We can start by defining the terms:

$$\delta x_k \triangleq x_k - \hat{x}_k \tag{110}$$

$$\delta u_k \triangleq u_k - \hat{u}_k \tag{111}$$

From which we can define a set of trust region slack variables $\{\eta_k\}_{k=1}^N \in \mathbb{R}$ where the following constraint is applied:

$$\delta x_k^\top \delta x_k + \delta u_k^\top \delta u_k \leq \eta_k \tag{112}$$

Additionally, we can apply a virtual control slack augmentation to the linearized-discretized dynamics, given by variable $\mu_k \in \mathbb{R}^{n_x}$:

$$x_{k+1} = A_k x_k + B_k^- \nu_k + B_k^+ \nu_{k+1} + z_k + \mu_k \tag{113}$$

We can construct a shorthand where, for a temporal variable $\xi(\tau) \in \mathbb{R}^n$ discretized into a set $\{\xi_k\}_{k=1}^N$, we denote $\bar{\xi} \triangleq [\xi_1^\top, \ldots, \xi_N^\top]^\top \in \mathbb{R}^{nN}$, where $\bar{\xi}_k$ extracts ξ_k from $\bar{\xi}$. Then, we can construct the following PTR objective function:

$$\underset{\bar{x}, \bar{\nu}, \bar{\eta}, \bar{\mu}}{\text{minimize}} \quad w_{\mathcal{O}} \mathcal{J}_{\mathcal{O}}(\bar{x}, \bar{\nu}) + w_\eta \mathcal{J}_\eta(\bar{\eta}) + w_\mu \mathcal{J}_\mu(\bar{\mu}) \tag{114}$$

Where we have the following components:

$$\mathcal{J}_{\mathcal{O}}(\bar{x}, \bar{\nu}) \triangleq \phi(\bar{x}_N) + \sum_{k=1}^{N} \Gamma(\bar{x}_k, \bar{\nu}_k) \tag{115}$$

$$\mathcal{J}_\eta(\bar{\eta}) \triangleq \|\bar{\eta}\|_2 \tag{116}$$

$$\mathcal{J}_\mu(\bar{\mu}) \triangleq \|\bar{\mu}\|_1 \tag{117}$$

With $\{w_{\mathcal{O}}, w_\eta, w_\mu\} \in \mathbb{R}_{++}$ being associated weighting components.

D. The PTR Subproblem

With all aforementioned structure in place, we can assert the convexified discrete-time subproblem used in traditional PTR algorithms; a summary is provided in problem 118. It is also important to note that, in regards to the compound STC constraints presented in III.F, we denote (k_j^+, k_j^-) as the indices corresponding to $(\tau_{k,j}^+, \tau_{k,j}^-)$.

Convex Discrete-Time Problem (118)

Objective:

$$\underset{\bar{x},\bar{\nu},\bar{\eta},\bar{\mu}}{\text{minimize}} \quad w_{\mathcal{O}}\mathcal{J}_{\mathcal{O}}(\bar{x},\bar{\nu}) + w_{\eta}\mathcal{J}_{\eta}(\bar{\eta}) + w_{\mu}\mathcal{J}_{\mu}(\bar{\mu}) \tag{118a}$$

subject to: (118b)

Dynamics:

$$x_{k+1} = A_k x_k + B_k^- \nu_k + B_k^+ \nu_{k+1} + z_k + \mu_k \quad \forall k \in [N-1] \tag{118c}$$

State Constraints:

$$\|v_{\mathcal{I}}(\tau_k)\| \leq v_{\max} \quad \forall k \in [N] \tag{118d}$$
$$\|\omega_{\mathcal{I}}(\tau_k)\| \leq \omega_{\max} \quad \forall k \in [N] \tag{118e}$$
$$e_z^\top r_{\mathcal{I}}(\tau_k) \geq 0 \quad \forall k \in [N] \tag{118f}$$

Control Constraints:

$$\|T_{\mathcal{B}}(\tau_k)\| \leq T_{\max} \quad \forall k \in [N] \tag{118g}$$
$$\|M_{\mathcal{B}}(\tau_k)\| \leq M_{\max} \quad \forall k \in [N] \tag{118h}$$
$$T_{\min} \leq \Xi(\hat{T}_{\mathcal{B}}(\tau_k))^\top T_{\mathcal{B}}(\tau_k) \quad \forall k \in [N] \tag{118i}$$
$$e_x^\top T_{\mathcal{B}}(\tau_k) \geq 0 \quad \forall k \in [N] \tag{118j}$$
$$e_y^\top T_{\mathcal{B}}(\tau_k) = e_z^\top T_{\mathcal{B}}(\tau_k) = 0 \quad \forall k \in [N] \tag{118k}$$

Scanning STCs:

for $j \in [n_{\text{scan}}]$ (118l)

$$C^1(\tau_k)\left(x(\tau_k) - \hat{x}(\tau_k)\right) + c^1(\hat{x}(\tau_k)) \leq 0 \quad \forall k \in [k_j^+, k_j^-] \tag{118m}$$
$$C^2(\tau_k)\left(x(\tau_k) - \hat{x}(\tau_k)\right) + c^2(\hat{x}(\tau_k)) \leq 0 \quad \forall k \in [k_j^+, k_j^-] \tag{118n}$$
$$\mathcal{T}(g_j^+, g_j^-, k_j^+, k_j^-) \leq 0 \tag{118o}$$

end (118p)

Boundary Conditions:

$$m(0) = m_0, \quad m(1) \geq m_{\min} \tag{118q}$$
$$r_{\mathcal{I}}(0) = r_0, \quad r_{\mathcal{I}}(1) = r_f \tag{118r}$$
$$v_{\mathcal{I}}(0) = v_0, \quad v_{\mathcal{I}}(1) = v_f \tag{118s}$$
$$\omega_{\mathcal{B}}(0) = \omega_0, \quad \omega_{\mathcal{B}}(1) = \omega_f \tag{118t}$$
$$\Xi(\hat{q}_{\mathcal{I}\to\mathcal{B}}(0))^\top q_{\mathcal{I}\to\mathcal{B}}(0) = 1 \tag{118u}$$

Trust Region:

$$\delta x_k^\top \delta x_k + \delta u_k^\top \delta u_k \leq \eta_k \quad \forall k \in [N] \tag{118v}$$
(118w)

E. The PTR Algorithm

In this paper, we consider the same iterative PTR algorithm as mentioned in [21, 36], with termination criteria on both the trust region and virtual control as follows:

$$\mathcal{J}_{\eta}(\bar{\eta}) \leq \epsilon_{\eta} \tag{119}$$
$$\mathcal{J}_{\mu}(\bar{\mu}) \leq \epsilon_{\mu} \tag{120}$$

Notably, however, rather than using the linear interpolation initialization outlined in e.g. [21], we present a new approach to producing an accurate initial guess for this specific problem structure. In practice, this new initialization has shown to produce stronger convergence properties, and is – in many cases – necessary to converge to a solution at all. We start by using the *lossless convexification* approach introduced in [1–4] to produce a 3-DOF powered descent guidance solution. That is to say, we encode all relevant constraints from 55 on states $m(t), r_{\mathcal{I}}(t), v_{\mathcal{I}}(t)$ and control $T_{\mathcal{I}}(t)$ (notably defined in the inertial frame), with the introduction of a lossless convexification constraint to replace (31). Notably, this does not include the scanning STC constraints, as

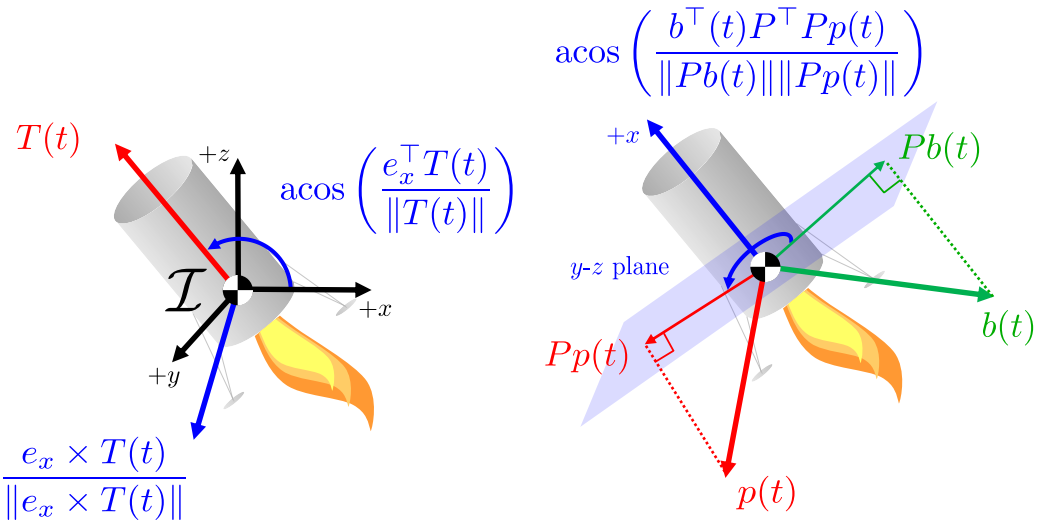

Fig. 3 This diagram illustrates the necessary steps to derive a proximal 6-DOF attitude profile from a 3-DOF solution as given by section V.E, with the tilt restriction on the left, and roll restriction on the right.

these must be imposed on the attitude DCM $\mathcal{R}_{\mathcal{I}\to\mathcal{B}}(t)$ (derived from $q_{\mathcal{I}\to\mathcal{B}}(t)$). Additionally, while the lossless convexification formulation is *fixed-final-time*, a higher-level line-search can be implemented to find a solution paired with an optimal time-of-flight.

Next, we would like to convert this 3-DOF problem into a *proximal* 6-DOF problem, starting with the attitude of the vehicle parameterized (in this case) by $q_{\mathcal{I}\to\mathcal{B}}(t)$. A two-step process can be used to define the body frame $\mathcal{B}$ relative to the inertial frame $\mathcal{I}$ in the 3-DOF context. We will consider the construction of a unit quaternion q by a rotation angle-axis pair $(\theta, \hat{n})$, where $q \triangleq [\cos(\theta/2), \sin(\theta/2)\hat{n}^\top]^\top$.

1. Tilt restriction. We start by considering an intermediate frame $\mathcal{B}'$, where we apply a *shortest-arc rotation* from inertial $+x$ to $T_{\mathcal{I}}(t)$, hence constraining the vehicle's $+x$ (tilt) axis. Then, we can define $q_{\mathcal{I}\to\mathcal{B}'}(t)$ with angle-axis pair:

$$\theta_{\mathcal{I}\to\mathcal{B}'} = \text{acos}\left(\frac{e_x^\top T_{\mathcal{I}}(t)}{\|T_{\mathcal{I}}(t)\|}\right) \tag{121}$$

$$\hat{n}_{\mathcal{I}\to\mathcal{B}'} = \frac{[e_x\times]T_{\mathcal{I}}(t)}{\|[e_x\times]T_{\mathcal{I}}(t)\|} \tag{122}$$

2. Roll restriction. Next, in the frame $\mathcal{B}'$, we would like to roll the vehicle about the $+x$ axis such that the boresight vector $b_{\mathcal{B}'}(t)$ is as closed aligned with a desired pointing direction $p_{\mathcal{B}'}(t)$ as possible. To do this, we can project $b_{\mathcal{B}'}(t)$ and $p_{\mathcal{B}'}(t)$ to the $\mathcal{B}'$ y-z plane with a matrix P, defined as:

$$P \triangleq \begin{bmatrix} 0 & 1 & 0 \\ 0 & 0 & 1 \end{bmatrix} \tag{123}$$

Consequently, the closest alignment is achieved when the boresight projection $Pb_{\mathcal{B}'}(t)$ is *aligned* with desired projection $Pp_{\mathcal{B}'}(t)$. This secondary transformation will result in the final proximal body-frame definition $\mathcal{B}$, defined by $q_{\mathcal{B}'\to\mathcal{B}}(t)$ with angle-axis pair:

$$\theta_{\mathcal{B}'\to\mathcal{B}} = \text{acos}\left(\frac{b_{\mathcal{B}'}^\top(t)P^T Pp_{\mathcal{B}'}(t)}{\|Pb_{\mathcal{B}'}(t)\|\|Pp_{\mathcal{B}'}(t)\|}\right) \tag{124}$$

$$\hat{n}_{\mathcal{B}'\to\mathcal{B}} = e_x \tag{125}$$

Then, we have that the proximal attitude realization $q_{\mathcal{I}\to\mathcal{B}}(t) = q_{\mathcal{I}\to\mathcal{B}'}(t) \otimes q_{\mathcal{B}'\to\mathcal{B}}(t)$. An illustration of these transformations is displayed in Fig. 3. An important followup question can be asked: *how do we obtain* $p_{\mathcal{B}'}(t)$? With consideration of the scanning events mentioned in III.F, we can apply the following logic:

- **During an event:** if $t \in [t_j^+, t_j^-]$ for any $j \in [n_{\text{scan}}]$, simply point towards the centroid of the event scanning region, such that $p_{\mathcal{B}'}(t) = z_{\mathcal{B}'}^j - r_{\mathcal{B}'}(t)$.

Table 2 Terrain scanning scenario parameters.

Parameter	Value	Parameter	Value
m_0	1500 kg	$m_{\min}$	750 kg
r_0	$[4000, 600, 3000]^\top$ m	r_f	$[0, 0, 0]^\top$ m
v_0	$[-60, 30 - 30]^\top$ m/s	v_f	$[0, 0, 0]^\top$ m/s
ω_0	$[0, 0, 0]^\top{}^\circ$/s	ω_f	$[0, 0, 0]^\top{}^\circ$/s
$T_{\min}$	600 N	$v_{\max}$	90 m/s
$T_{\max}$	3000 N	$\omega_{\max}$	5°/s
$M_{\max}$	50 N · s		
I_{sp}	300 s	$J_{\mathcal{B}}$	$\text{diag}([0.6, 4.2, 4.2])$ kg · m^2
g_0	9.81 m/s^2	β	20°
$g_{\mathcal{I}}$	$-[1.625, 0, 0]^\top$ m/s^2	$b_{\mathcal{B}}$	$[-\sqrt{3}/2, 0, 0.5]^\top$
N	30	$w_{\mathcal{O}}$	1e − 1
ϵ_η	1e − 6	w_η	1e2
ϵ_μ	1e − 6	w_μ	1e3

- **Between events:** If $t \in (t_j^-, t_{j+1}^+)$ for any $j \in [n_{\text{scan}} - 1]$, perform a spherical interpolation on $p_{\mathcal{B}'}(t)$ between $p_{\mathcal{B}'}(t_j^-)$ and $p_{\mathcal{B}'}(t_{j+1}^+)$ with interpolation fraction $f = (t - t_j^-)/(t_{j+1}^+ - t_j^-)$.
- **Before the first event:** If $t \in [0, t_1^+)$, hold first event pointing direction $p_{\mathcal{B}'}(t) = p_{\mathcal{B}'}(t_1^+)$.
- **After the last event:** If $t \in (t_{n_{\text{scan}}}^-, t_f]$, hold last event pointing direction $p_{\mathcal{B}'}(t) = p_{\mathcal{B}'}(t_{n_{\text{scan}}}^-)$.

We note that this approach assumes events do not overlap, which can be enforced by appropriate construction of the trigger functions and times. From this, we can use equations (4) and (5) (or their discrete-time counterparts in the case of initial guess generation for PTR) to compute the angular velocity profile $\omega_{\mathcal{B}}(t)$. Consequently, equation (5) can be used to obtain the moment profile $M_{\mathcal{B}}(t)$ as well. However, these can also be interpolated between boundary conditions or set to zero; the quaternion attitude profile is most critical to obtaining a reliable initial guess for this problem class.

VI. Simulation Results

In this section, we introduce a practical scenario in regards to perception-based exploration of a planetary terrain environment during a powered descent guidance maneuver. Specifically, we consider a mission objective wherein a reference vehicle is commanded to scan different terrain regions while descending, with each scanning event triggered in a different altitude envelope above ground. In the following subsections, we will discuss parameterization of this scenario and assess simulation results.

A. Scenario Parameterization

The aforementioned scenario will consider three separate (non-overlapping) terrain scanning events $n_{\text{scan}} = 3$, with each trigger based strictly on the altitude of the vehicle. Moreover, for an event $j \in [n_{\text{scan}}]$, we consider the following constraint functions:

$$g_j^+(r_{\mathcal{I}}(t)) = e_z^\top r_{\mathcal{I}}(t) - h_j^+$$
$$g_j^-(r_{\mathcal{I}}(t)) = e_z^\top r_{\mathcal{I}}(t) - h_j^-$$

Under this definition, the following terrain scanning STC parameters are considered:

Scan 1:	$h_1^+ = 2500$ m,	$h_1^- = 2100$ m,	$\rho^1 = 500$ m,	$z_{\mathcal{I}}^1 = [3000, 1000, 0]^\top$ m
Scan 2:	$h_2^+ = 1700$ m,	$h_2^- = 1300$ m,	$\rho^2 = 300$ m,	$z_{\mathcal{I}}^2 = [2000, -1000, 0]^\top$ m
Scan 3:	$h_3^+ = 900$ m,	$h_3^- = 500$ m,	$\rho^3 = 100$ m,	$z_{\mathcal{I}}^3 = [1000, 0, 0]^\top$ m

Additionally, the trigger indices k_j^+ and k_j^-, $j \in [n_{\text{scan}}]$, are chosen to be uniformly distributed across the interval $k \in [1, N]$, but not such that the outer events start at the endpoints of the interval. Moreover, we can construct a vector of indices $K \in \mathbb{R}^{N+2}$ which stores uniform linear interpolations between 1 and N over $N + 2$ elements (with rounding to the nearest integer for each element), from which we can assign the values:

$$\{K_2, \ldots, K_{N+1}\} \to \{k_1^+, k_1^-, \ldots, k_{n_{\text{scan}}}^+, k_{n_{\text{scan}}}^-\}$$

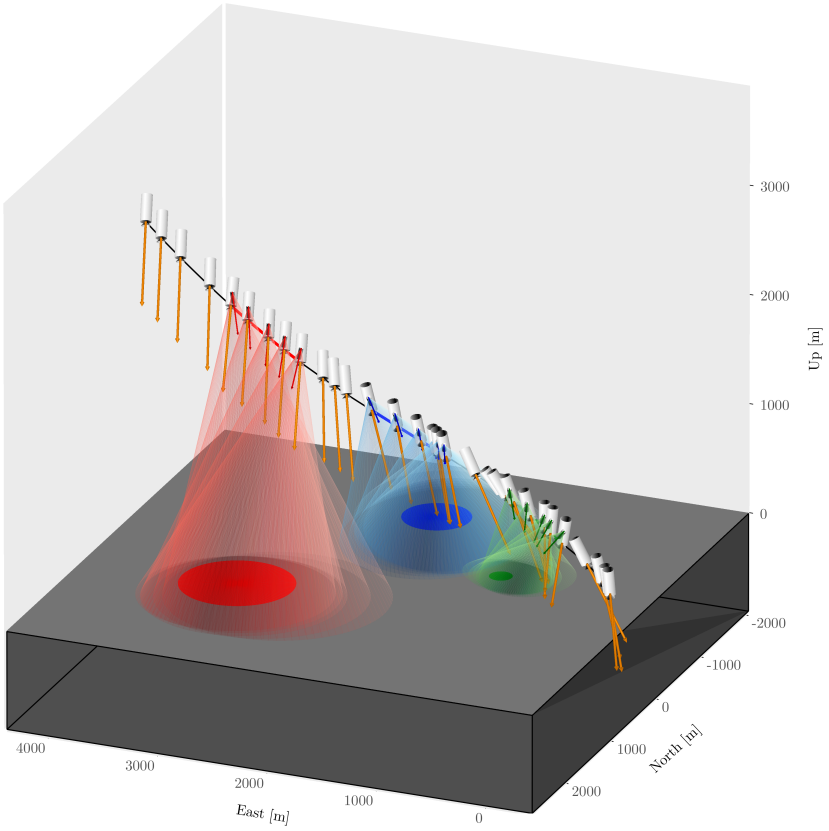

Fig. 4 This figure presents a visualization of the vehicle trajectory and terrain scan events in regards to the candidate powered descent guidance scenario introduced in section VI. The vehicle is depicted with a gray cylindrical body at each solver knot point, along with an orange arrow corresponding to the (normalized) thrust vector. Terrain scanning events 1-3 are colored red, blue, and green, respectively, with the boresight pointing vector, FOV cone and target region color-coded. Additionally, the simulated trajectory is displayed in black, with colored segments during the activation of each scanning event.

This trigger node allocation heuristic has been (empirically) proven to work well for many scenario variations in this problem class. We also consider a minimum-cumulative-thrust objective for this problem, such that:

$$\mathcal{J}_{\mathcal{O}}(\bar{x}, \bar{\nu}) = \sum_{k=1}^{N} \|T_{\mathcal{B},k}\|$$

Where $T_{\mathcal{B},k}$ is extracted from the first three elements of $\bar{\nu}_k$. All other scenario parameters are presented in Table 2.

B. Analysis & Discussion

From Fig. 4, a visualization of the vehicle maneuver can be seen, including the solver output at each knot point, as well as the simulated continuous-time solution (using fourth order Runge-Kutta integration). The solution was obtained on a 2023 Razer Blade 15" laptop[†] using the JuMP (Julia programming language) parser [40] and open-source ECOS second-order cone program solver [41], achieving a net solve time of 4.35 seconds over 19 PTR iterations with $N = 30$ nodes. From the aforementioned figure, it can be visually observed that all scanning targets are kept within view (as shown by the overlayed conic projections onto the surface). To validate that this is indeed the case, we can define the *maximum visibility angle*, γ, which records the maximum angle between the boresight vector $b_{\mathcal{I}}(t)$ and all feasible[‡] relative directions to points within the target set $\mathcal{Z}_{\text{circ}}$. More formally, this term is defined as:

$$\gamma = \max \left\{ \text{acos}\left(\frac{(\tilde{z} - r_{\mathcal{I}}(t))^{\top} b_{\mathcal{I}}}{\|\tilde{z} - r_{\mathcal{I}}(t)\|} \right), \ \forall \tilde{z} \in \mathcal{Z}_{\text{circ}} \right\}$$

[†]This laptop has an AMD Ryzen 9 6900HX CPU with 3301 Mhz clock speed and 8 cores.
[‡]In practice, we uniformly sample points about the circumference of $\mathcal{Z}_{\text{circ}}$ to approximately compute the maximum.

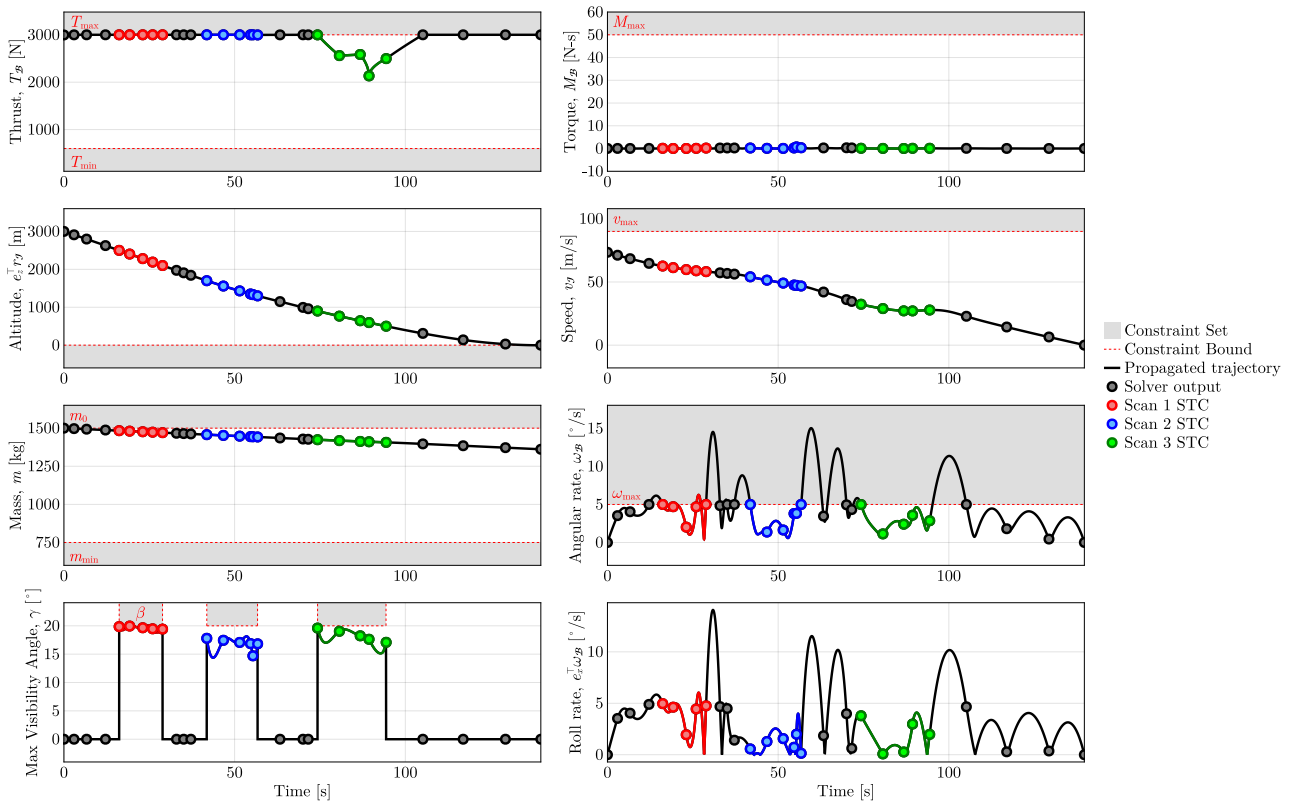

Fig. 5 This figure presents various time signals of interest in regards to the candidate powered descent guidance scenario introduced in section VI, with color-coded scan events and constraint bounds.

From Fig. 5, we can observe this signal $\gamma(t)$ for all three scanning events, and see that it falls below the required threshold, which is equivalent to the FOV half-angle, β. It would appear that the constraint is activated in the first scan, however, upon closer inspection, there is indeed a small gap explained by the conservatism of the $\mathcal{Z}_{\text{ball}}$ set approximation (as highlighted in section III.C). All other signals are validated to satisfy their required constraints at the discretized knot points, however in some cases, we can observe non-trivial intersample constraint violation between knot points. Particularly in regards to the angular rate $\omega_{\mathcal{B}}(t)$, intersample constraint violations between pointing events are of large violation magnitude. Upon further inspection, it can be seen that these violations are concentrated on the roll rate $e_x^\top \omega_{\mathcal{B}}(t)$, suggesting that the violations are a result of large roll transition requirements between scanning events.

There exists multiple possible remedies to this. A constraint could be applied directly to the roll rate to reduce it further at the knot points, however the potential for large violations still exists. The practitioner may choose to instead space the pointing events further apart temporally (such as mandating a minimum amount of time between events), or design the sensor/target configuration to reduce the required amount of rolling between events. All of these solutions are heuristic, however – future research will target more explicit methods to reduce intersample constraint violation.

VII. Conclusion

This paper presents a novel optimal control formulation, termed Constrained Visibility Guidance (CVG), which outlines a viable approach to model complex terrain scanning maneuvers coupled with traditional powered descent guidance objectives. Important future work includes modeling and resolving intersample constraint violations in the discrete-time optimal control problem, and further improving solver time performance for real-time usage on capacity-constrained hardware. Additionally, constraint modeling extensions can be considered to generalize beyond a circle-shaped region of interest to more complex geometries.

VIII. Acknowledgement

The authors would like to thank Purnanand Elango from the UW Autonomous Controls Laboratory for his contributions towards the control-augmented time-interval dilation formulation, and Chris Owens from Astrobotic Technology for his assistance in proving the constrained conic intersections theorem. This material is based upon

work supported in part by the National Science Foundation Graduate Research Fellowship Program under Grant No. DGE-2140004, as well as by the Office of Naval Research grants N00014-16-1-2877 and N00014-16-1-3144.

References

[1] Acikmese, B., and Ploen, S. R., "Convex programming approach to powered descent guidance for mars landing," *Journal of Guidance, Control, and Dynamics*, Vol. 30, No. 5, 2007, pp. 1353–1366.

[2] Açıkmeşe, B., and Blackmore, L., "Lossless convexification of a class of optimal control problems with non-convex control constraints," *Automatica*, Vol. 47, No. 2, 2011, pp. 341–347.

[3] Blackmore, L., Açıkmeşe, B., and Carson III, J. M., "Lossless convexification of control constraints for a class of nonlinear optimal control problems," *Systems & Control Letters*, Vol. 61, No. 8, 2012, pp. 863–870.

[4] Açıkmeşe, B., Carson, J. M., and Blackmore, L., "Lossless convexification of nonconvex control bound and pointing constraints of the soft landing optimal control problem," *IEEE Transactions on Control Systems Technology*, Vol. 21, No. 6, 2013, pp. 2104–2113.

[5] Harris, M. W., and Açıkmeşe, B., "Lossless convexification for a class of optimal control problems with quadratic state constraints," *2013 American Control Conference*, IEEE, 2013, pp. 3415–3420.

[6] Harris, M. W., and Açıkmeşe, B., "Lossless convexification of non-convex optimal control problems for state constrained linear systems," *Automatica*, Vol. 50, No. 9, 2014, pp. 2304–2311.

[7] Dueri, D., Açıkmeşe, B., Scharf, D. P., and Harris, M. W., "Customized real-time interior-point methods for onboard powered-descent guidance," *Journal of Guidance, Control, and Dynamics*, Vol. 40, No. 2, 2017, pp. 197–212.

[8] Dueri, D. A., "Real-time optimization in aerospace systems," Ph.D. thesis, 2018.

[9] Acikmese, B., Casoliva, J., Carson, J., and Blackmore, L., "G-fold: A real-time implementable fuel optimal large divert guidance algorithm for planetary pinpoint landing," *Concepts and Approaches for Mars Exploration*, Vol. 1679, 2012, p. 4193.

[10] Acikmese, B., Aung, M., Casoliva, J., Mohan, S., Johnson, A., Scharf, D., Masten, D., Scotkin, J., Wolf, A., and Regehr, M. W., "Flight testing of trajectories computed by G-FOLD: Fuel optimal large divert guidance algorithm for planetary landing," *AAS/AIAA spaceflight mechanics meeting*, 2013, p. 386.

[11] Scharf, D. P., Açıkmeşe, B., Dueri, D., Benito, J., and Casoliva, J., "Implementation and experimental demonstration of onboard powered-descent guidance," *Journal of Guidance, Control, and Dynamics*, Vol. 40, No. 2, 2017, pp. 213–229.

[12] Malyuta, D., Szmuk, M., and Acikmese, B., "Lossless convexification of non-convex optimal control problems with disjoint semi-continuous inputs," *arXiv preprint arXiv:1902.02726*, 2019.

[13] Malyuta, D., and Açikmeşe, B., "Lossless convexification of optimal control problems with semi-continuous inputs," *IFAC-PapersOnLine*, Vol. 53, No. 2, 2020, pp. 6843–6850.

[14] Kunhippurayil, S., Harris, M. W., and Jansson, O., "Lossless convexification of optimal control problems with annular control constraints," *Automatica*, Vol. 133, 2021, p. 109848.

[15] Mao, Y., Szmuk, M., and Açıkmeşe, B., "Successive convexification of non-convex optimal control problems and its convergence properties," *2016 IEEE 55th Conference on Decision and Control (CDC)*, IEEE, 2016, pp. 3636–3641.

[16] Mao, Y., Szmuk, M., Xu, X., and Açikmese, B., "Successive convexification: A superlinearly convergent algorithm for non-convex optimal control problems," *arXiv preprint arXiv:1804.06539*, 2018.

[17] Alonso-Mora, J., Baker, S., and Rus, D., "Multi-robot navigation in formation via sequential convex programming," *2015 IEEE/RSJ International Conference on Intelligent Robots and Systems (IROS)*, IEEE, 2015, pp. 4634–4641.

[18] Matiussi Ramalho, G., Carvalho, S. R., Finardi, E. C., and Moreno, U. F., "Trajectory optimization using sequential convex programming with collision avoidance," *Journal of Control, Automation and Electrical Systems*, Vol. 29, 2018, pp. 318–327.

[19] Bonalli, R., Cauligi, A., Bylard, A., and Pavone, M., "Gusto: Guaranteed sequential trajectory optimization via sequential convex programming," *2019 International conference on robotics and automation (ICRA)*, IEEE, 2019, pp. 6741–6747.

[20] Szmuk, M., Eren, U., and Acikmese, B., "Successive convexification for mars 6-dof powered descent landing guidance," *AIAA Guidance, Navigation, and Control Conference*, 2017, p. 1500.

[21] Szmuk, M., and Acikmese, B., "Successive convexification for 6-dof mars rocket powered landing with free-final-time," *2018 AIAA Guidance, Navigation, and Control Conference*, 2018, p. 0617.

[22] Szmuk, M., Reynolds, T. P., and Açıkmeşe, B., "Successive convexification for real-time six-degree-of-freedom powered descent guidance with state-triggered constraints," *Journal of Guidance, Control, and Dynamics*, Vol. 43, No. 8, 2020, pp. 1399–1413.

[23] Reynolds, T. P., Szmuk, M., Malyuta, D., Mesbahi, M., Açıkmeşe, B., and Carson III, J. M., "Dual quaternion-based powered descent guidance with state-triggered constraints," *Journal of Guidance, Control, and Dynamics*, Vol. 43, No. 9, 2020, pp. 1584–1599.

[24] Szmuk, M., Acikmese, B., and Berning, A. W., "Successive convexification for fuel-optimal powered landing with aerodynamic drag and non-convex constraints," *AIAA Guidance, Navigation, and Control Conference*, 2016, p. 0378.

[25] Lysandrou, P., and Braun, R. D., "A 6-DoF Successive Convexification Powered Descent Guidance Implementation using Modified Rodrigues Parameters," *AIAA Scitech 2021 Forum*, 2021, p. 0861.

[26] Lee, U., and Mesbahi, M., "Dual quaternions, rigid body mechanics, and powered-descent guidance," *2012 ieee 51st ieee conference on decision and control (cdc)*, IEEE, 2012, pp. 3386–3391.

[27] Lee, U., and Mesbahi, M., "Optimal power descent guidance with 6-DoF line of sight constraints via unit dual quaternions," *AIAA Guidance, Navigation, and Control Conference*, 2015, p. 0319.

[28] Lee, U., and Mesbahi, M., "Constrained autonomous precision landing via dual quaternions and model predictive control," *Journal of Guidance, Control, and Dynamics*, Vol. 40, No. 2, 2017, pp. 292–308.

[29] Carson, J. M., Munk, M. M., Sostaric, R. R., Estes, J. N., Amzajerdian, F., Blair, J. B., Rutishauser, D. K., Restrepo, C. I., Dwyer-Cianciolo, A. M., Chen, G., et al., "The SPLICE project: Continuing NASA development of GN&C technologies for safe and precise landing," *AIAA SciTech 2019 forum*, 2019, p. 0660.

[30] Dinh, Q. T., and Diehl, M., "Local convergence of sequential convex programming for nonconvex optimization," *Recent Advances in Optimization and its Applications in Engineering: The 14th Belgian-French-German Conference on Optimization*, Springer, 2010, pp. 93–102.

[31] Malyuta, D., Reynolds, T., Szmuk, M., Mesbahi, M., Acikmese, B., and Carson, J. M., "Discretization performance and accuracy analysis for the rocket powered descent guidance problem," *AIAA Scitech 2019 Forum*, 2019, p. 0925.

[32] Reynolds, T. P., and Mesbahi, M., "The crawling phenomenon in sequential convex programming," *2020 American Control Conference (ACC)*, IEEE, 2020, pp. 3613–3618.

[33] Kamath, A. G., Elango, P., Yu, Y., Mceowen, S., Chari, G. M., Carson III, J. M., and Açıkmeşe, B., "Real-Time Sequential Conic Optimization for Multi-Phase Rocket Landing Guidance," *IFAC-PapersOnLine*, Vol. 56, No. 2, 2023, pp. 3118–3125.

[34] Kamath, A. G., Elango, P., Kim, T., Mceowen, S., Yu, Y., Carson, J. M., Mesbahi, M., and Acikmese, B., "Customized real-time first-order methods for onboard dual quaternion-based 6-DoF powered-descent guidance," *AIAA SciTech 2023 Forum*, 2023, p. 2003.

[35] Yu, Y., Elango, P., Topcu, U., and Açıkmeşe, B., "Proportional–integral projected gradient method for conic optimization," *Automatica*, Vol. 142, 2022, p. 110359.

[36] Malyuta, D., Reynolds, T. P., Szmuk, M., Lew, T., Bonalli, R., Pavone, M., and Açıkmeşe, B., "< Convex Optimization for Trajectory Generation: A Tutorial on Generating Dynamically Feasible Trajectories Reliably and Efficiently," *IEEE Control Systems Magazine*, Vol. 42, No. 5, 2022, pp. 40–113.

[37] Malyuta, D., Yu, Y., Elango, P., and Açıkmeşe, B., "Advances in trajectory optimization for space vehicle control," *Annual Reviews in Control*, Vol. 52, 2021, pp. 282–315.

[38] Shaffer, J., Owens, C., Klein, T., Horchler, A., Buckner, S. C., Acikmese, B., Johnson, B., and Carson, J. M., "Implementation and Testing of Convex Optimization-based Guidance for Hazard Detection and Avoidance on a Lunar Lander," *AIAA SciTech 2024 forum*, 2024.

[39] Teo, K., Jennings, L., Lee, H. W. J., and Rehbock, V., "The control parameterization enhancing transform for constrained optimal control problems," *The ANZIAM Journal*, Vol. 40, No. 3, 1999, pp. 314–335.

[40] Dunning, I., Huchette, J., and Lubin, M., "JuMP: A modeling language for mathematical optimization," *SIAM review*, Vol. 59, No. 2, 2017, pp. 295–320.

[41] Domahidi, A., Chu, E., and Boyd, S., "ECOS: An SOCP solver for embedded systems," *2013 European control conference (ECC)*, IEEE, 2013, pp. 3071–3076.